ORIGINAL RESEARCH ARTICLE

Self-organizing vascularized subchondral bone organoids from stromal vascular fraction enable functional osteochondral interface regeneration

Tao Qian[1†], Jiazhou Wu[2†], Zexian Liu[2,3†], Aiyuan Wang[2], Yanbin Wu[2], Junli Wang[1], Hongyu Jiang[2], Zhengrui Zhou[2], Cheng Huang[2], Yazhou Li[2], Junming Zhang[1], Biao Ma[1], Yun Bai[1], Jialiang You[2], Endong Luo[2], Dingkai Wang[2], Ying He[2*], and Jiang Peng[1,2*]

[1]The Third Clinical College, Jinzhou Medical University, Jinzhou, Liaoning Province, China

[2]Institute of Orthopedics, The Fourth Medical Center of Chinese PLA General Hospital, Beijing Key Laboratory of Regenerative Medicine in Orthopedics, Key Laboratory of Musculoskeletal Trauma & War Injuries, PLA, Beijing, Beijing Municipality, China

[3]Graduate School, Chinese PLA General Hospital, Beijing, Beijing Municipality, China

***Corresponding authors:** Jiang Peng (pengjiang301@126.com); Ying He (251032611@qq.com)

[†]*These authors contributed equally to this work.*

Citation: Qian T, Wu J, Liu Z, *et al*. Self-organizing vascularized subchondral bone organoids from stromal vascular fraction enable functional osteochondral interface regeneration. *Organoid Res*. 2025;1(4):025480037. doi: 10.36922/OR025480037

Received: November 30, 2025

Revised: December 22, 2025

Accepted: December 25, 2025

Abstract

Osteoarthritis (OA) is closely associated with subchondral bone (SCB) degeneration; however, current models fail to adequately mimic its complex microenvironment. Here, we developed a self-organizing subchondral bone organoid (SSBO) by co-culturing stromal vascular fraction (SVF) cells with decellularized cartilage extracellular matrix (CECM). SVF provided cellular heterogeneity, including adipose-derived stem cells (ADSCs), endothelial cells, pericytes, and macrophages, while CECM served as a native scaffold with tissue-specific cues. SSBO exhibited spontaneous spheroid formation, active cellular infiltration, and dynamic matrix remodeling. Compared to ADSC-only controls, SSBO showed enhanced cell viability, vascularization, collagen remodeling, and spatial organization. Immunostaining and qPCR analyses confirmed an endochondral ossification-like process, characterized by the sequential expression of SOX9, COL2A1, RUNX2, COL1A1, and OCN. In vivo implantation into immunodeficient mice demonstrated robust angiogenesis, bone-like tissue formation, and integration with host vasculature. Furthermore, in a mouse osteochondral defect model, SSBO significantly promoted repair, with improved bone volume, trabecular architecture, and cartilage regeneration. Collectively, this study presents a novel strategy for constructing vascularized, immunomodulatory, and osteogenic SCB organoids, offering a promising platform for regenerative medicine and bone–cartilage interface repair.

Keywords: SVF; Organoids; Tissue engineering; Stromal vascular fraction; Subchondral bone

1. Introduction

Osteoarthritis (OA) is one of the most common degenerative joint diseases worldwide. It severely affects patients' quality of life.[1,2] With the aging of the population, the incidence of OA continues to rise. It has become a major public health concern and a socioeconomic burden.[3] Typical pathological features of OA include cartilage degeneration, abnormal remodeling of the subchondral bone (SCB), and synovial inflammation.[4,5] For a long time, OA was thought to affect articular cartilage primarily. However, recent studies have shown that SCB also plays a key role in OA onset and progression.[6,7] Clinical and basic research suggest that abnormal SCB remodeling often occurs before cartilage degeneration. Changes in SCB structure and function can impair nutrient supply and mechanical support to the overlying cartilage. In addition, SCB may contribute to OA progression through abnormal signaling pathways.[8,9] Therefore, restoring the structure and function of SCB is considered a potential target for OA treatment. It may offer a new strategy for early intervention and disease reversal.[10]

SCB lies beneath the articular cartilage. It consists of a dense bone plate and a network of trabecular bone. SCB plays key biological and mechanical roles.[11,12] It supports the cartilage and provides it with nutrients. It also acts as a hub for signal transmission and regulation at the bone-cartilage interface.[13,14] The structure of SCB is highly complex. It includes bone-related cells such as osteoblasts, osteocytes, and osteoclasts. It also contains endothelial cells, immune cells, and stromal cells. Together, they form a dynamic "bone–vascular–immune" system.[14-16] This system is essential for joint homeostasis, bone remodeling, blood flow regulation, and immune response. In diseases such as OA, an imbalance in the SCB microenvironment can lead to trabecular disruption, abnormal blood vessel growth, and increased local inflammation. These changes form a vicious cycle that worsens cartilage damage and speeds up disease progression.[17-19] Although tissue engineering has made progress in bone regeneration, current strategies still cannot fully mimic the complex microenvironment of SCB.[12]

In recent years, organoid technology has opened new paths for modeling and regenerating complex tissues *in vitro*.[20] Organoids are 3D tissue structures derived from adult stem cells or pluripotent stem cells. They are cultured under specific conditions to mimic the structure and function of real organs.[21] Since Sato *et al.* first established intestinal organoids in 2009, this technology has been widely applied in disease modeling, drug screening, and regenerative medicine for various organs, including the liver,[22] brain,[23] and kidney.[24] The main advantage of organoids is their ability to recreate complex cell types, spatial organization, and functional features *in vitro*. This greatly improves the physiological relevance and application potential of traditional tissue models. It also offers a new way to mimic the complex structure of SCB.[25] However, no current studies have developed SCB organoids for regenerative repair. In particular, there is still no 3D model that combines key functions such as vascularization, bone remodeling, and immune regulation.

SVF is a heterogeneous cell population rich in various cell types. It includes ADSCs, endothelial progenitor cells, smooth muscle cells, and macrophages.[26] Studies have shown that endothelial progenitor cells in SVF have strong angiogenic capacity. They can rapidly form vascular networks in ischemic or hypoxic environments.[26] ADSCs and macrophages also support angiogenesis by secreting pro-angiogenic factors such as VEGF and FGF, thereby improving local microcirculation.[27] More importantly, SVF has immunomodulatory properties. Its endogenous cells can secrete anti-inflammatory factors, thereby reducing inflammation and creating a favorable microenvironment for tissue repair.[28] Therefore, SVF not only helps establish a vascularized microenvironment but also provides nutritional and signaling support for osteogenic cell growth and differentiation. It is a promising cell source for building organoids with both vascularization and immune-regulation functions.

To better mimic the complex SCB and support multicellular assembly, this study used cartilage extracellular matrix (CECM) as the scaffold material for organoid construction. CECM is derived from decellularized cartilage tissue. It retains key matrix components such as collagen, glycosaminoglycans, and various endogenous bioactive factors. It shows good biocompatibility and tissue-inductive properties.[29,30] Previous studies have shown that CECM provides stable physical support for stem cell adhesion, growth, and self-organization. Its natural matrix structure and biochemical signals also promote spatial organization and functional integration among cells. This helps recreate a physiologically relevant 3D microenvironment.[31-33] Therefore, CECM is a promising scaffold for reconstructing the structure and function of the SCB region. It is an ideal biomaterial choice for *in vitro* modeling of SCB organoids.[34]

Based on this rationale, we developed a patient-derived subchondral bone organoid (SSBO) model by co-culturing SVF cells with CECM. According to established definitions, organoids are three-dimensional (3D) structures derived from stem or progenitor cells. They exhibit self-organization, include multiple cell types, and recapitulate key structural and functional features of native tissue. Unlike conventional 3D spheroids, which are typically homogenous and lack spatial organization, or scaffold-based constructs that require external signals and pre-designed patterns, SSBO formation depends on the intrinsic heterogeneity of SVF and the bioactive properties of CECM. This combination enables spontaneous self-organization, self-differentiation, and the emergence of spatially patterned functional domains. SVF contains a mixture of ADSCs, endothelial cells, pericytes, and immune-regulatory cells. CECM provides native cartilage-derived structural and biochemical cues that promote regeneration. Together, they support the assembly of a complex 3D structure without the need for added growth factors or engineered signaling environments. As a result, SSBO exhibits essential organoid characteristics, including cellular heterogeneity, layered architecture, and functional biomimicry. *In vitro*, SSBO developed a trabecular-like structure with vascular channels. Functionally, it demonstrated enhanced osteogenesis, angiogenesis, and immunomodulation. To evaluate the role of SVF cellular diversity, we established a control group by co-culturing purified ADSCs with

CECM (designated as the AM group). We compared both groups in terms of structural organization, vascularization, bone regeneration, and immune regulation. In a rat model of subchondral bone defect, SSBO showed improved tissue repair, highlighting its translational potential for regenerating the bone–cartilage interface. In conclusion, we propose a self-organizing strategy for constructing subchondral bone organoids using SVF and CECM. This approach provides a novel organoid-based platform for osteochondral tissue regeneration.

2. Materials and methods

2.1. Materials isolation and culture of SVF and hADSCs

The procedures for isolating and culturing stromal vascular fraction (SVF) and adipose-derived stem cells (ADSCs) received ethical clearance from the Ethics Committee of the Fourth Medical Center, PLA General Hospital (Approval No. 2023KY088-KS001). Subcutaneous fat samples were obtained from patients undergoing hip replacement surgery. To isolate the intermediate fat layer, the adipose tissue collected via liposuction was subjected to centrifugation at 900 rpm for a duration of 60 seconds.A 5 mL aliquot of the fat was transferred to Tube 1, and then the cells were counted, while the remaining fat was labeled as Tube 2. Add 0.1 mg/mL Liberase collagenase(Roche, Switzerland) to both tubes and incubate in a 37°C water bath for 45 minutes. The enzymatic activity was inhibited by introducing a culture medium that included a serum substitute. This was followed by centrifugation at 1500 rpm for 10 minutes to separate the components. The resulting cell pellet was then collected and resuspended in a small volume of MSC-T4 medium, which is based on the serum substitute. Finally, the suspension was filtered using a 100 μm cell strainer to ensure the removal of remaining debris. Cells collected from Tube 1 were lysed with red blood cell lysis buffer and counted to determine the total cell number in Tube 2. The cell suspension from Tube 2 was adjusted to a final seeding density of 300,000 cells per well in a 96-well U-bottom plate. Each well received 200 μL of culture medium.

Additionally, cells from Tube 1 were seeded into multiple 75 cm^2 culture flasks and cultured at 37 °C in an environment containing 5% CO_2. Once they reached a confluence of 80–90%, primary hADSCs (P0) were harvested using trypsin and reseeded at the same cell density in 96-well U-bottom plates. The SVF and ADSCs were extracted from the same donor and analyzed in parallel to ensure consistency.

2.2. Cell composition detection

The cellular composition of SVF and primary ADSCs was characterized through flow cytometry. Briefly, the cells were centrifuged, after which the SVF and primary ADSC single-cell suspensions were adjusted to a concentration of 10^6/mL and separated into seven 1.5 mL EP tubes labeled A to G, with 0.2 mL per tube. Tube A contained a cocktail of primary antibodies against CD31, CD34, CD45, CD73, and CD90. Tubes B-F served as single-color compensation controls, containing individual antibodies against CD31, CD34, CD45, CD73, and CD90, respectively, whereas tube G contained PBS serving as the blank control. Next, live/dead dye was added to the cells, followed by incubation in the dark at room temperature for 30 minutes. This was followed by washing and centrifugation twice; the samples were analyzed through flow cytometry, and the data were processed using FlowJo software. Each experiment is repeated three times.

The gating strategy is illustrated in Supplementary Figure S1. Singlets were first gated using FSC-A vs. FSC-H parameters, followed by selection of viable cells based on live/dead staining.CD45 expression was used to separate CD45$^+$ leukocytes from CD45$^-$ stromal cells. Within the CD45$^-$ population, ADSCs were defined as CD90$^+$CD73$^+$, EPCs as CD34$^+$CD31$^+$, and pericytes as CD146$^+$CD90$^-$CD73$^-$.CD45$^+$ cells were collectively defined as leukocytes. Subpopulation percentages were calculated based on the total number of live singlet events.

2.3. Preparation of CECM microparticles

Fresh porcine articular cartilage was harvested and mechanically fragmented. A section of the fragmented cartilage was reserved and assigned to the native cartilage group without further treatment. The remaining cartilage fragments underwent repeated freeze–thaw cycles, using trypsin and nuclease. The resulting suspension was subjected to differential centrifugation to extract cartilage particles. Residual chemical agents were thoroughly removed through repeated washing with PBS. The cartilage particles were filtered using 180 μm and 300 μm sieves to prepare microparticles with a size range of 180–300 μm. The final CECM microparticles were sterilized using the cobalt-60 (Co-60) gamma irradiation and stored at 4 °C until use.2.3.1.

2.4. Histological and DAPI staining

Cartilage particles, both untreated and decellularized, were immersed in a tissue fixative solution (Solarbio, China) for 30 minutes. After fixation, the samples were embedded and sliced into 5 μm sections using a Leica cryostat (Germany). Hematoxylin and eosin (H&E) staining (Solarbio, China) was utilized to evaluate the overall tissue architecture and morphological features. To highlight the distribution of proteoglycans within the extracellular matrix (ECM), Alcian Blue staining (Solarbio, China) was performed. The nuclei of residual or infiltrated cells were identified via DAPI staining (Solarbio, China).

2.5. Quantification of DNA

DNA was extracted from the samples using the QIAamp DNA Mini Kit (Product No. 56304, Qiagen, Germany) and then quantified using the Quant-iT PicoGreen dsDNA Quantitation Kit (Product No. P7589, Invitrogen) following the manufacturer's instructions. Next, the Fluorescence intensity was detected at an excitation wavelength of 480 nm and an emission wavelength of 520 nm using the Infinite 200 Pro system (TECAN). The concentration of the DNA was determined from a standard curve.

2.6. Scanning electron microscopy (SEM)

To ensure structural preservation, the CECM microparticles were immersed in 2.5% glutaraldehyde (Solarbio, China) for 24 hours and subsequently washed three times with phosphate-buffered saline (PBS). A graded ethanol series was used to dehydrate the samples. The morphology and surface features of the microparticles were then observed and imaged using scanning electron microscopy (SEM) (Thermo Fisher Scientific, USA), following the guidelines provided by the manufacturer.

2.7. Construction of callus organoids

To prepare callus organoids, CECM microparticles were added to the low-adhesion 96-well U-bottom plates containing the previously seeded cells at a ratio of 1×10^5 cells per mg of microparticles, with 3 mg of microparticles per well. The cell cultures were conducted at 37 °C with 5% CO_2 in complete MSC-T4 medium (supplemented with a serum substitute). Half of the medium was replaced every two days. The formation of spheroids was monitored during the first four days post-seeding at specific time points: 0 h, 24 h, 48 h, 72 h, and 96 h. The development of two groups was examined on Day 0, Day 7, Day 14, and Day 21, with Day 0 defined as the time point when compact spheroids had formed—i.e., 96 hours after initial seeding.

Day 14 was selected as the primary observation time point based on preliminary assessments of cell viability, morphological organization, and early matrix deposition. This time point also corresponds to a biologically relevant phase in endochondral ossification, during which vascularization and mineralization are typically initiated. Therefore, it was used as a representative stage for in-depth characterization of SSBO development.

2.8. Cytoskeleton and nuclear visualization

Organoids from both experimental groups underwent fixation followed by cryosectioning into slices measuring 5 μm in thickness. They were then stained with antibodies against α-tubulin (1:200, Abcam, UK) and nuclear counterstaining with DAPI (Invitrogen, USA) to visualize the cytoskeletal organization within organoids through immunofluorescence staining. Fluorescent signals were detected using a fluorescence microscope to characterize the cytoskeletal distribution and nuclear morphology.

2.9. Cell viability and apoptosis assessment

Cell viability within the organoid spheroids at days -4, 0, 7, 14, and 21 is assessed using the PrestoBlue™ Cell Viability Reagent (Invitrogen, USA), following the manufacturer's instructions. A volume of PrestoBlue equivalent to 10% of the culture medium (20 μL per well) is added to the organoid-containing plates and incubated at 37 °C with 5% CO_2 for 1 hour. The supernatant is then collected, and fluorescence intensity is measured. Quantitative analysis is performed according to the manufacturer's protocol, and cell viability was normalized to that of the SSBO at day −4.

Additionally, organoids from both groups at days -4, 0, 7, 14, and 21 are fixed, cryosectioned into 5 μm slices, and subjected to terminal deoxynucleotidyl transferase dUTP nick end labeling (TUNEL) staining using a commercial kit (Beyotime, China) to detect apoptotic cells, following the manufacturer's instructions. Quantification of the apoptotic signal is conducted using ImageJ software.

2.10. Transmission electron microscope (TEM)

After 14 days of spheroid formation in both experimental groups, samples were collected for further processing. The samples were fixed in 2.5% glutaraldehyde for 24 hours at 4 °C. Subsequently, they were rinsed with phosphate-buffered saline (PBS) and The samples were subsequently treated with 1% osmium tetroxide to enhance membrane contrast for 1 hour. Dehydration was carried out through a graded ethanol series and acetone. Finally, the samples were embedded, sectioned into ultrathin slices, stained with uranyl acetate and lead citrate, air-dried, and examined using a transmission electron microscope (TEM).

2.11. Quantitative real-time PCR (qRT-PCR)

To measure the gene expression during the differentiation process of both types of organoids, qRT-PCR was conducted on samples collected at Day 0, Day 7 and Day 14 following spheroid formation. The expression levels of chondrogenic markers (SOX9, COL2A1), osteogenic markers (COL10A1, RUNX2, COL1A1, OCN), Inflammation-related markers (IL-1β, IL-10) and angiogenic markers (VEGF, CD31) were quantified using The sequences of the primers are listed in Table S1.

Total RNA was isolated from organoids at Day 0, Day 7 and Day 14 using a total RNA isolation kit (Vazyme, China). The RNA was reverse-transcribed into cDNA using the HiScript® RT kit (Vazyme, China). qRT-PCR amplification was performed with the SYBR® qPCR Master Mix (Vazyme, China) on a real-time PCR system. Finally, the expression of target mRNA was calculated using the

2^−ΔΔCT method and normalized to the expression of GAPDH as the internal control.

2.12. Osteogenic induction and ALP/alizarin red staining

SSBO and AM were transferred to osteogenic induction medium on day 4 post-spheroid formation. Half of the medium was replaced daily. Samples were collected at Day 7, Day 14, and Day 21. Following treatment with 4% paraformaldehyde and subsequent immersion in 30% sucrose for cryoprotection, the specimens were embedded in OCT for cryosectioning compound and cryosectioned at a thickness of five μm for subsequent staining. Each group is repeated three times at each time point. Quantitative analysis of staining intensity was normalized to the positive signal of AM at day 7, which served as a control.

ALP Staining: Alkaline phosphatase activity was detected using the BCIP/NBT staining kit (Beyotime, China). Samples were incubated with the working solution at room temperature in the dark for 5–30 minutes until color development. After staining, sections were rinsed with distilled water, mounted using neutral resin, and imaged using a panoramic confocal digital slide scanner.

Alizarin Red Staining: Calcium deposition was assessed using Alizarin Red S staining. Samples were incubated with Alizarin Red S solution at room temperature for 10 minutes, followed by three washes with PBS. After dehydration and mounting with neutral resin, images were acquired using a panoramic confocal digital slide scanner.

2.13. Immunofluorescence staining

The organoids obtained from both groups were fixed and cryosectioned into five μm-thick slices. The overall structure and protein expression profiles during organoid differentiation at days 0, 7, and 14 are assessed using the Seven-Colour Multiplex Fluorescence Staining Kit Plus (Boster Biological Technology, China), following the manufacturer's instructions. The following primary antibodies were used: CD44(1:200, Abcam, UK),CD68(1:200, Abcam, UK),CD45(1:200, Abcam, UK),PDGFR(1:200, Abcam, UK), CD31 (1:200, Abcam, UK), SOX9 (1:200, Abcam, UK), COL2A1 (1:200, Invitrogen, USA), COL10A1 (1:200, Invitrogen, USA), IL-1β (1:200, Invitrogen, USA), IL-10 (1:200, Invitrogen, USA) and COL1A1 (1:200, Abcam, UK).

2.14. *In vivo* implantation and regenerative tissue evaluation

Six-week-old male BALB/c nude mice with immunodeficiency were randomly assigned into two experimental groups: the SSBO group and the AM group (n = 4 per group). Anesthesia was induced via intraperitoneal injection of 0.3% sodium pentobarbital. A dorsal midline incision approximately 1 cm in length was made, and two subcutaneous pockets were formed through blunt dissection techniques. The pre-fabricated organoid constructs were carefully inserted into these pockets, and the skin was closed using 6-0 surgical sutures (Ethicon, USA). After a 3-week implantation period, the animals were euthanized, and the implanted materials were retrieved, fixed overnight in 4% paraformaldehyde, and subjected to subsequent histological and molecular analyses, including hematoxylin and eosin (H&E) staining, Masson's trichrome, immunofluorescence, and immunohistochemistry.

In a separate set of experiments, eight-week-old male BALB/c nude mice were randomly distributed into four groups (n = 4 each): Control (untreated), AM, SSBO, and Sham. Mice were anesthetized with 0.3% sodium pentobarbital prior to surgery. A medial skin incision was made to access the knee joint, exposing the patellar tendon and medial collateral ligament. This was followed by an incision in the joint capsule, and the knee was gently flexed to reveal the femoral trochlear groove. In the Sham group, the patella was temporarily dislocated and repositioned, followed by layered closure of the capsule, muscle, and skin. For the remaining groups, a standardized osteochondral defect was created by vertically inserting a 0.8 mm diameter round-tipped needle—with a positioning bead placed 1 mm from the tip—into the trochlear groove and rotating it gently. Organoid constructs were then implanted into the defect sites in the AM and SSBO groups, while the Control group received no intervention. All incisions were closed in layers. After 4 weeks, mice were euthanized, and their femurs were collected for gross morphological evaluation. The specimens were subsequently fixed overnight in 4% paraformaldehyde and analyzed using micro-computed tomography (Micro-CT), immunohistochemistry, and various histological stains including H&E, Masson's trichrome, and Safranin O.

All procedures involving animals were conducted in accordance with the NIH Guidelines for the Care and Use of Laboratory Animals and were approved by the Institutional Animal Care and Use Committee (IACUC) of Yuma Bio Co., Ltd. (Beijing, China) under protocol number SYXK20250023.

2.15. Statistical analysis

All statistical analyses were performed using GraphPad Prism 10 (GraphPad Software, USA). Quantitative data are presented as mean ± standard deviation (SD) from at least three independent biological replicates. Data normality was assessed using the Shapiro–Wilk test. For comparisons between two groups, unpaired two-tailed Student's t-test was used for normally distributed data, while the Mann–Whitney U test was applied otherwise. For multiple group comparisons, one-way analysis of variance (ANOVA) followed by Tukey's post hoc test was used for normally distributed data; otherwise, the Kruskal–Wallis test was applied. A *p*-value of < 0.05 was considered statistically significant. Exact *p*-values are reported in the Results section where applicable.

3. Results

3.1. Construction of organoids

Freshly isolated human SVF cells and *in vitro* expanded primary ADSCs were examined through flow cytometry to identify cellular subpopulations and measure their relative proportions (Figure S1A, B). Scatter diagrams of flow cytometric results (Figure 1A and B) and flow cytometric quantitative analysis (Figure S1C) demonstrated that the proportion of adipose-derived mesenchymal stem cells ($CD45^{-}CD73^{+}/CD90^{+}$) was significantly enriched in the cultured ADSCs (99.37±0.12%) compared to their proportion in SVF (23.15±11.08%)($p<0.0001$). The proportions of endothelial progenitor cells ($CD45^{-}CD31^{-}/CD34^{+}$) and pericytes ($CD45^{-}CD73^{-}/CD90^{-}/CD146^{+}$) in cultured ADSCs were (0.03 ± 0.03%) and (0.00 ± 0.00%), respectively, which were both lower than the corresponding values in the SVF group (1.36 ± 1.15% and 1.42 ± 0.62%, respectively); Despite observable variation, the results did not demonstrate statistical significance. Notably, the leukocyte population ($CD45^{+}$) was significantly reduced in cultured ADSCs (0.27±0.14%) relative to SVF (69.1±8.29%)($p<0.0001$).

The porcine cartilage was decellularized, ground, and sequentially filtered through 150 μm and 300 μm mesh filters to obtain CECM microcarriers with particle sizes ranging from 150 to 300 μm. Results of the histological and DAPI staining demonstrated that the decellularization was successful, as no visible nuclei were seen within the lacunae of the CECM group relative to the native cartilage group, while the majority of the ECM was retained (Fig. S2A). DNA quantification also indicated successful nuclear removal (Fig. S2B) ($p<0.0001$). Analysis of the SEM images showed that the surface of the CECM microcarriers was porous and rich in collagen fibers (Fig. S2C). Collectively, these results confirm that the CECM microcarriers possess the potential to support cell adhesion and facilitate intercellular interactions. Next, the cells and CECM were seeded into low-adhesion 96-well plates for co-culture. The cells formed tight envelopes around the CECM and self-assembled into compact. spheroidal aggregates within 4 days (Figure 1C).

To evaluate the morphological characteristics of the callus organoids, microtubule staining was conducted (Figure 1D). The results indicated that the organoids exhibited a well-defined spherical morphology, with microtubules enriched along the luminal surface forming continuous ring-like structures. The contours of the organoids appeared smooth and intact, lacking signs of collapse.

3.2. Analysis of organoid viability and structural features

To evaluate cell viability within the organoids, a PrestoBlue assay was performed for quantitative analysis (Figure 2A). The results showed that the AM group exhibited higher metabolic activity at the early stage of culture, likely due to their strong proliferative capacity during the prior 2D culture. However, after transfer to the 3D environment, their viability declined, with a brief increase observed between days 7 and 14. In contrast, the SSBO group showed lower initial metabolic activity, possibly due to recent enzymatic digestion. However, viability recovered rapidly from day 0 after spheroid formation and remained consistently higher than that of the AM group. By day 21, both groups showed a decline in viability. Overall, SSBO maintained significantly higher cell viability throughout the culture period, suggesting more potent biological activity. TUNEL staining further confirmed these findings (Figure 2B and C). Although apoptosis increased over time in both groups, the SSBO group consistently showed a lower proportion of apoptotic cells, supporting its superior cell viability.

H&E staining was performed on day 14 organoids (Figure S3A). In the AM group, cells were mainly distributed on the outer surface of the CECM particles, with limited infiltration into the interior. The structure of the CECM remained largely intact. In contrast, the SSBO group showed tighter integration between cells and the CECM. A large number of cells migrated into the matrix, accompanied by noticeable degradation of the CECM.To further investigate the interaction between cells and the CECM, transmission electron microscopy (TEM) was performed on day 14 organoids. In the AM group, most cells were attached to the CECM surface without deep infiltration (Figure 2D).

In contrast, the SSBO group cells penetrated into the interior of the CECM particles. Some cells exhibited pseudopodia-like protrusions that extended into the matrix, indicating active participation in scaffold remodeling rather than passive embedding, suggesting strong matrix-penetrating ability (Figure 2E). Notably, the CECM in the SSBO group showed extensive degradation and disorganized collagen fibers, with significantly lower collagen content compared to the AM group. This may result from the synergistic activity of multiple cell types in SSBO, which promotes the active degradation and utilization of the CECM.In addition, abundant collagen fibers were observed around the cells near the CECM in the SSBO group, markedly more than in the AM group (Figures 2F and G). Quantitative analysis showed that

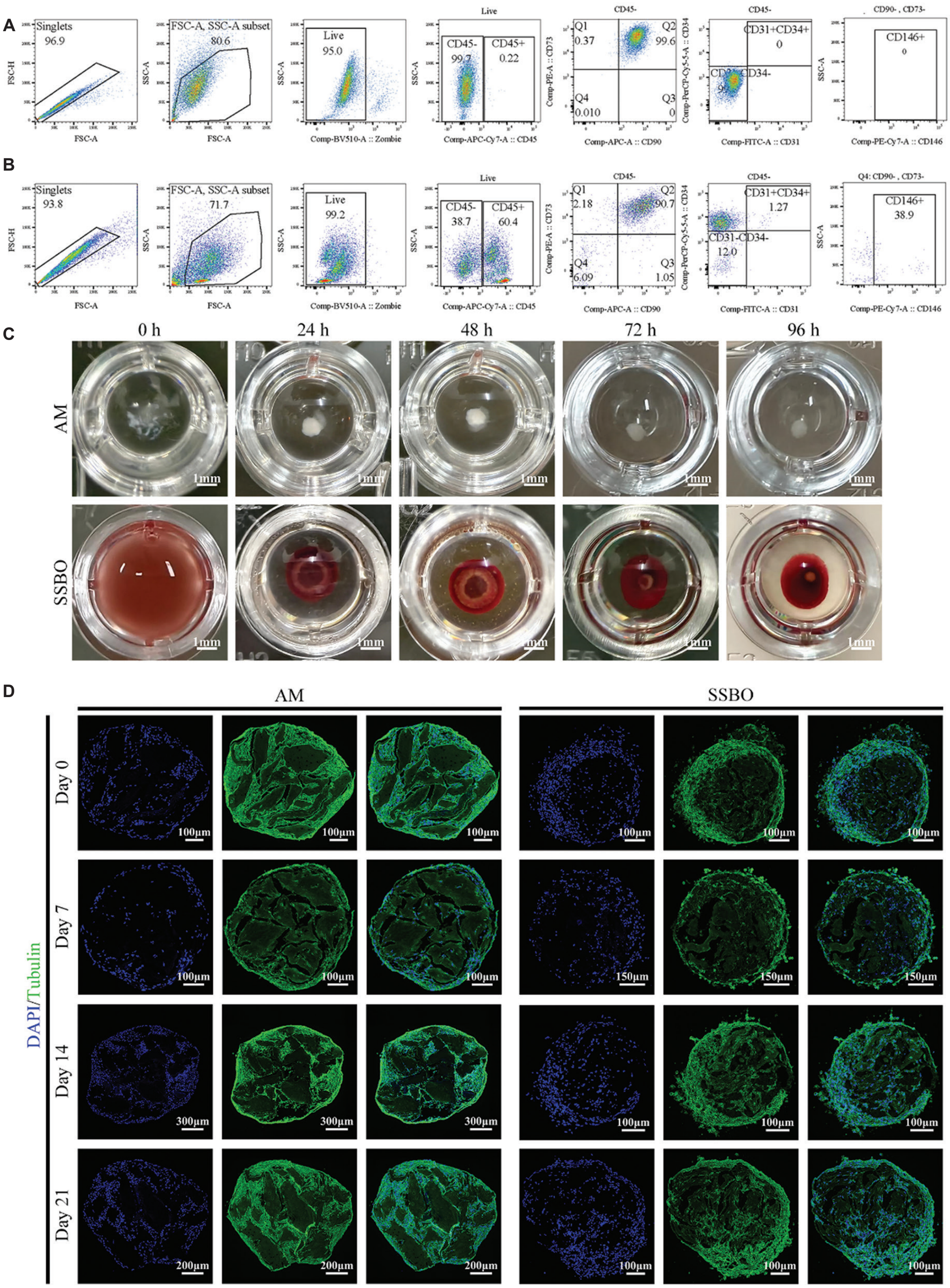

Figure 1. Construction of Organoids. (A) Flow cytometric analysis of P0 ADSCs. (B) Flow cytometric analysis of SVF. (C) Gross morphology of organoids after co-culture. (D) Immunofluorescence staining of organoids showing structural organization

the SSBO group had a significantly higher collagen fiber density than the AM group ($p = 0.0057$). The average fiber diameter was also larger in the SSBO group (Figures S3B). These observations suggest that SVF-derived cells may

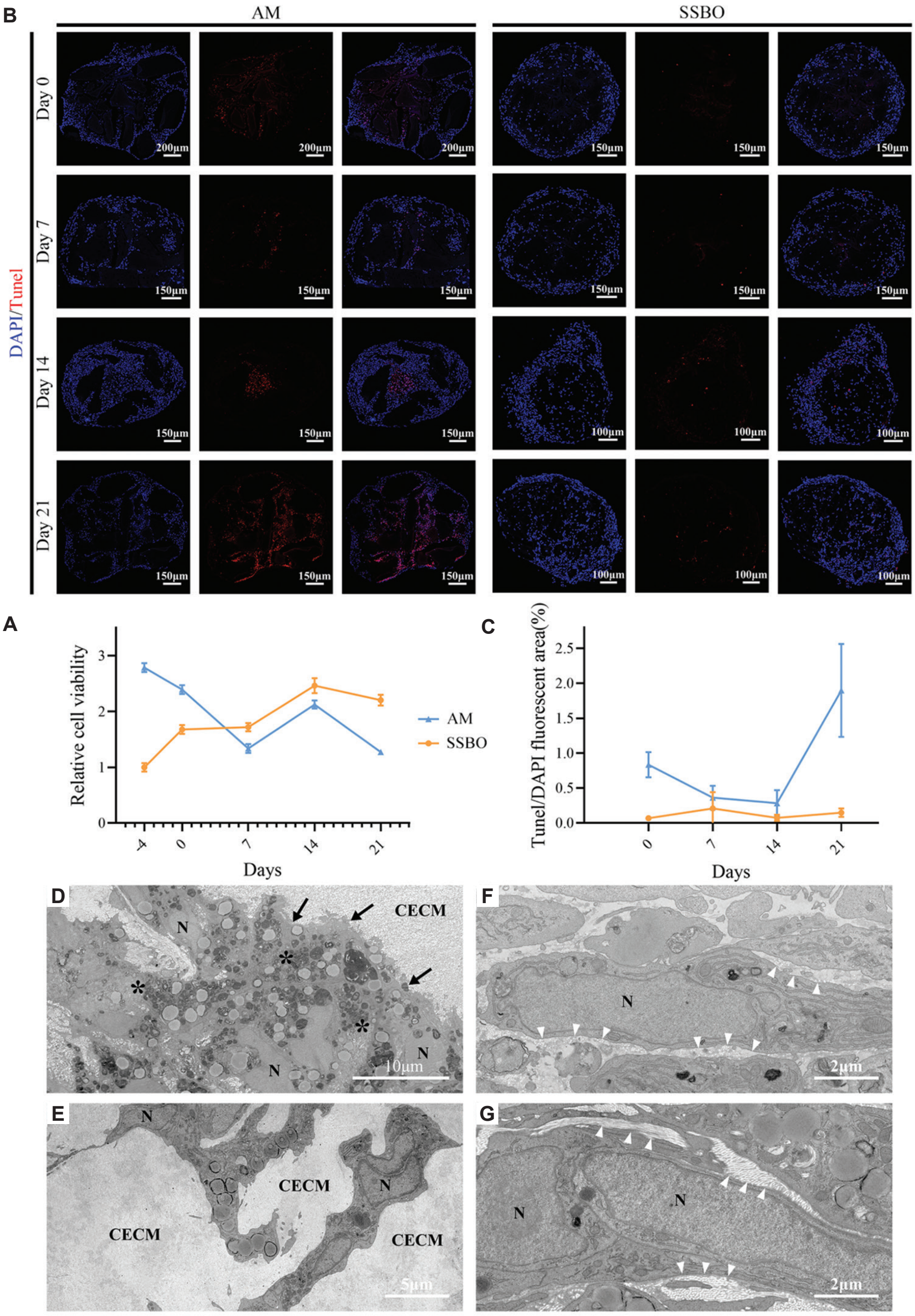

Figure 2. The vitality and structure of organoids. (A) Cell viability analysis using PrestoBlue assay. Values were normalized to the fluorescence signal of freshly seeded SVF cells, which served as the baseline reference due to equal initial cell seeding density across all groups. (B) TUNEL immunofluorescence staining to assess apoptosis.(C) Quantification of TUNEL-positive signal normalized to DAPI fluorescence area. (D) and (F) show transmission electron microscopy (TEM) images of the AM group after 14 days of culture. (E) and (G) show TEM images of the SSBO group after 14 days of culture. Black arrows indicate the boundary between CECM and the cells. Asterisks (*) mark nearby lysosomes. White arrowheads point to collagen fibers. "N" indicates the cell nucleus

actively degrade and absorb key CECM components (such as collagen), which are then used for extracellular matrix remodeling or biosynthesis. This mechanism may support cell differentiation, growth, and tissue repair—a hypothesis further verified in subsequent experiments. Moreover, AM group cells showed high lysosome content, suggesting a stressed or degenerative state. In contrast, SSBO cells contained abundant mitochondria and endoplasmic reticulum, with fewer lysosomes, indicating better cell function, higher metabolic activity, and overall improved biological performance (Figure S3C).

Next, we performed quantitative analysis of organoid size on day 14 (Figure S2D). The results showed that the overall size of the SSBO was smaller than that of the AM group. This may be due to two factors: (1) higher initial cell viability in the AM group, leading to greater cell proliferation; and (2) tighter integration between SVF cells and the CECM in the SSBO group. As a result, despite being seeded with the same number of cells, SSBO formed smaller organoids compared to AM.

3.3. Spatial organization and immunoregulatory characteristics of SSBO

To further characterize the cellular composition and spatial organization of SSBO organoids, we performed multiplex immunofluorescence co-staining at different time points (day 0, 7, and 14) (Figure 3A). At the early stage of spheroid formation (day 0), cells within SSBO were loosely arranged, lacking a clear tissue structure. As culture progressed, by day 14, the internal architecture became more organized. A dense, tubular network of endothelial progenitor cells was observed, primarily distributed around and along the surface of the CECM particles. The area of positive staining for these cells was significantly greater in the SSBO group than in the AM group, indicating stronger formation of a vascular-like structure in SSBO.

In contrast, AM organoids showed a simpler structure, mainly composed of scattered CD44-positive ADSCs, with a larger positive staining area than in SSBO (Figure 3B and C), reflecting lower cellular heterogeneity. Although ADSCs remained the dominant cell type in SSBO, other non-ADSC cell populations were also present, indicating clear cellular heterogeneity. PDGFR-positive pericytes were aligned in parallel with endothelial progenitor cells but showed no co-expression. The number of pericytes was slightly higher than that of endothelial cells (Figure 3D). To further assess neovascularization within the organoids, we performed quantitative analysis of $CD31^+$ vascular structures based on multiplex immunofluorescence images (Figure S4A). The SVF group showed significantly higher total vessel length and number of branch points compared to both the control and AM groups ($p < 0.0001$). This indicates that the SSBO group developed a denser and more complex vascular network. Such vascularization is essential for scaffold integration and tissue repair.

CD68 and CD45 double-positive macrophages were mainly located at the periphery of the organoids, with a significantly higher abundance in the SSBO group compared to the AM group (Figure 3D). Notably, cells migrating into the CECM interior were mainly ADSCs and macrophages, suggesting their key roles in scaffold attachment, remodeling, and microenvironment regulation. In summary, SSBO organoids gradually developed a structured spatial distribution during 3D culture, exhibiting clear cellular heterogeneity and functional compartmentalization at the tissue level.

In order to delineate the immunomodulatory function of macrophages in SSBO organoid assembly, expression of IL-1β and IL-10 was evaluated through immunofluorescence analysis (Figure S4B). The results showed that macrophages in SSBO predominantly expressed IL-10, with the IL-10-positive area significantly larger than that of IL-1β (Figures S4C, D), suggesting a polarization toward an anti-inflammatory M2 phenotype. We also conducted qPCR analysis of organoids at different time points (day 0, 7, and 14) (Figure S4E). In the SSBO group, IL-10 expression remained consistently high and was significantly elevated compared to the ADSC group throughout the culture period ($p<0.0001$). In contrast, IL-1β expression peaked briefly at day 0 in the SSBO group, then rapidly declined to near-baseline levels. This indicates a transient pro-inflammatory response during early spheroid formation, followed by rapid suppression. Further analysis of the IL-10/IL-1β ratio revealed a significant increase in SSBO at day 7, peaking, while the ADSC group maintained a low ratio throughout. These findings suggest that macrophages in SSBO may help maintain immune homeostasis and a regenerative microenvironment by promoting anti-inflammatory cytokine expression and suppressing pro-inflammatory signals. In summary, macrophages in SSBO exhibit an IL-10-dominant immunoregulatory profile, which may play a key role in tissue repair, matrix remodeling, and microenvironmental stability.

3.4. SSBO undergoes an endochondral ossification-like process *in vitro*

To dynamically track SSBO differentiation, we analyzed the expression of key lineage-related genes at days 0, 7, and 14 (Figure 4A). Both SSBO and the control group (AM) showed a trend toward chondrogenic differentiation, as indicated by the time-dependent upregulation of significant cartilage markers SOX9 and COL2A1. Notably, COL2A1 expression in the SSBO group was significantly higher than in the AM group at day 7, while SOX9 expression decreased after an initial peak, falling below that of the AM group. This suggests that SSBO may have transitioned from early-stage chondrogenesis to a more mature cartilage state. Interestingly, by day 14, SOX9 expression continued to rise in both groups, but remained significantly lower in SSBO compared to AM. Although this pattern does not fully align with the classical hypertrophic-phase dynamics of SOX9 in endochondral ossification, the deviation may be attributed to sustained signaling from the CECM

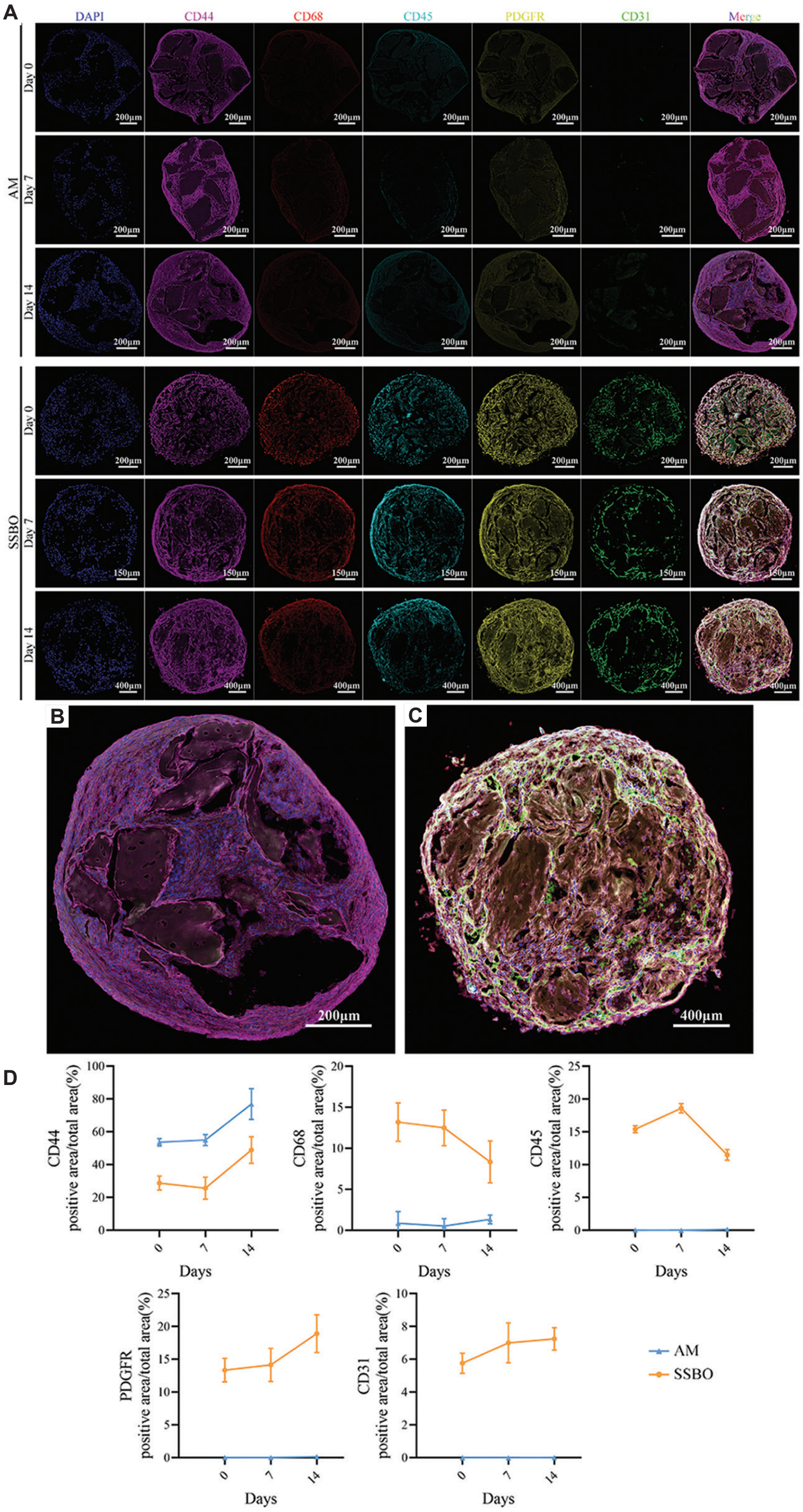

Figure 3. Spatial Distribution of Cells Within the Organoid. (A) Representative multicolor immunofluorescence images of SSBO and AM on days 0, 7, and 14 of culture. From left to right: nuclear staining (DAPI), adipose-derived mesenchymal stem cell marker (CD44), M0 macrophage marker (CD68), leukocyte marker (CD45), pericyte marker (PDGFR), endothelial cell marker (CD31), and merged images (Merge). (B) High-magnification view of AM on day 14 of spheroid formation. (C) High-magnification view of SSBO on day 14 of spheroid formation. (D) Quantification of the positive staining area (%) for each marker

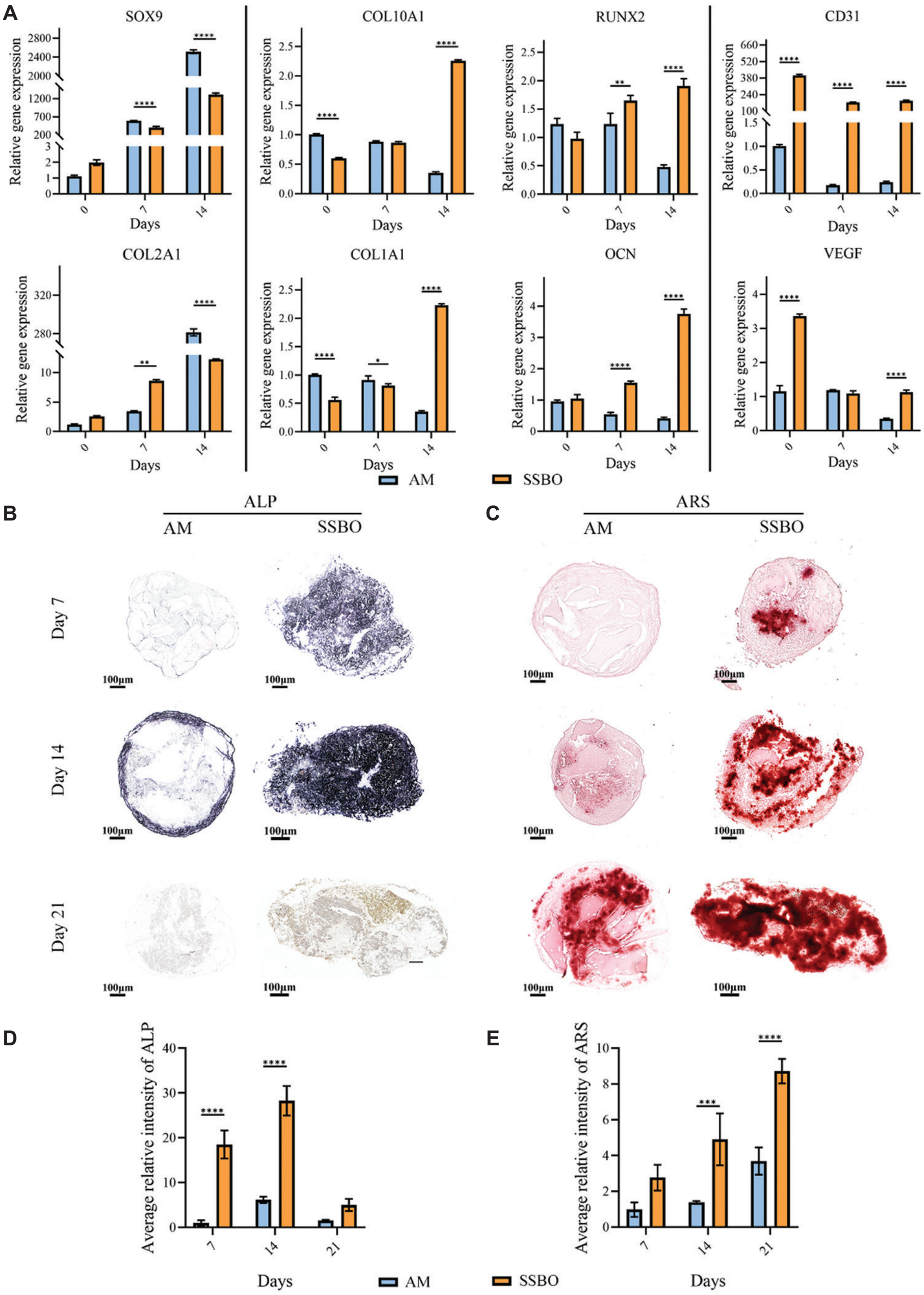

Figure 4. Differentiation of Organoids. (A) Quantitative PCR analysis of chondrogenic gene markers (SOX9, COL2A1), hypertrophic chondrocyte, and osteogenic markers (COL10A1, RUNX2, COL1A1, OCN) and angiogenic markers (CD31, VEGF) in both groups. Gene expression levels were normalized to the AM group at Day 0.(B)Alkaline phosphatase (ALP) staining of AM and SSBO at different time points during osteogenic induction. (C) Alizarin Red S staining of AM and SSBO at different time points during osteogenic induction. (D) Quantitative analysis of ALP staining normalized to AM on day 7 of osteogenic induction. (E)Quantitative analysis of Alizarin Red S staining normalized to AM on day 7 of osteogenic induction. All data are presented as the mean ± SD (*n*=3 biological replicates). Statistical significance: ns (not significant, p>0.05), $^{*}p<0.05$, $^{**}p<0.01$, $^{***}p<0.001$

microenvironment that promotes maintenance of the chondrogenic phenotype. Meanwhile, expression levels of COL10A1 (a hypertrophic cartilage marker), RUNX2 (an osteogenic transcription factor), COL1A1, and OCN (markers of mature osteogenesis) increased markedly over time in SSBO, especially at day 14. In contrast, these genes showed a declining trend in the AM group, suggesting that AM differentiation may have stalled at a stable chondrogenic phase. Together, these results indicate that SSBO undergoes a coordinated transition from cartilage to hypertrophic cartilage and then to bone, consistent with an endochondral ossification-like pathway, which closely resembles the physiological process of subchondral bone formation.

To further evaluate the angiogenic potential of SSBO, we analyzed the expression of vascular-related markers VEGF and CD31 (Figure 4A). During the early stage (days 0-7), both markers were downregulated in the SSBO group, possibly due to temporary suppression of vascular signaling by the CECM microenvironment. However, their expression began to increase from day 7 onward, suggesting progressive activation of angiogenic signaling during tissue maturation and the cartilage-to-bone transition. This pattern reflects a process of vascular reconstruction or re-initiation.In contrast, throughout the entire induction period, the expression levels of VEGF and CD31 in SSBO remained consistently higher than those in the AM group. The AM group, lacking vascular-related cell components, showed a continuous decline in both markers. These results indicate that the endothelial progenitor cells and pro-angiogenic factors enriched within SVF play a critical role in organoid assembly. They provide both structural and signaling support for the establishment of a vascularized microenvironment.

To further verify the osteogenic potential of the SSBO, osteogenic induction was performed for 0, 7, and 14 days, followed by alkaline phosphatase (ALP) and Alizarin Red staining (Figures 4B-E). The results showed that the SSBO group exhibited markedly higher ALP activity and more abundant calcium deposition, indicating significantly enhanced osteogenic capacity.

To further validate the differentiation process at the spatial level, multicolor immunofluorescence co-localization was performed to assess protein expression patterns in SSBO and AM organoids (Figure 5A). In the SSBO group, SOX9 expression gradually decreased starting from day 7, while COL2A1, COL10A1, and COL1A1 expressions progressively increased. These findings confirm that SSBO undergoes a sequential differentiation process *in vitro*, progressing from chondrogenesis to hypertrophy and, finally, to osteogenesis. In contrast, the AM group showed only a slight upregulation of COL2A1, with no significant changes in COL10A1 or COL1A1, suggesting that differentiation remained at the chondrogenic stage and lacked the capacity to progress toward osteogenesis. Furthermore, CD31 immunostaining revealed the progressive formation of abundant and well-organized vascular-like networks in the SSBO group, with signal intensity increasing over time (Figures 5B-D). In the AM group, CD31 expression remained minimal, and no similar vascular structures were observed. Interestingly, although CD31 mRNA expression showed only a modest increase in qPCR analysis, the protein exhibited pronounced spatial clustering and morphological organization within the tissue. This suggests that the formation of vascular-like structures in SSBO may depend more on cellular self-assembly and tissue remodeling rather than transcriptional upregulation alone. These observations further support the crucial role of endothelial progenitor cells within SVF in driving organoid self-organization and vascularization.

3.5. SSBO organoids form bone-like tissue and achieve vascular integration *in vivo* in immunodeficient mice

To evaluate the *in vivo* osteogenic potential of SSBO organoids and their ability to integrate with the host vasculature, four SSBO, pre-induced *in vitro* for 14 days, were co-cultured for 24 hours to promote fusion and form a stable, spheroid-like structure. These were then subcutaneously implanted into immunodeficient mice and harvested for analysis after 3 weeks (Figure 6A). Macroscopic observation revealed extensive vascular network formation around the SSBO implantation site, whereas AM organoids showed no visible vascular structures. This suggests that SSBO possess superior angiogenic potential and a greater capacity to integrate with host vasculature. Histological analysis further supported these findings. Hematoxylin and eosin (H&E) staining (Figure 6B) showed that SSBO implants maintained well-organized tissue architecture and uniform cellular distribution in vivo, with multiple vascular-like structures observed (Figure S5A). In contrast, the AM group displayed a looser tissue structure with minimal evidence of vascularization. Masson's trichrome staining (Figure 6C) revealed abundant blue-stained collagen fibers surrounding the SSBO organoids, arranged in a regular pattern indicative of mature bone-like tissue formation. In contrast, the AM group lacked significant collagen deposition, suggesting a limited capacity for bone-like tissue reconstruction *in vivo*.

To further validate the osteogenic differentiation potential of SSBO, we examined the expression of the late-stage osteogenic marker osteocalcin (OCN). Immunohistochemical staining (Figure 6D) revealed widespread and intense OCN-positive signals in the SSBO implantation sites, whereas the AM group exhibited significantly lower expression levels (Figure S5B) (p=0.001). These findings collectively confirm that SSBO organoids possess robust osteoinductive capacity in vivo. They can effectively integrate with the host vascular system and initiate the formation of bone-like tissue.

In addition, CD31 immunofluorescence staining (Figure 6E) confirmed in vivo vascularization within the organoid implants. In the SSBO group, a large number of human CD31-positive cells were observed, along with mouse CD31-positive cells, indicating the presence of chimeric vascular structures. These findings suggest that

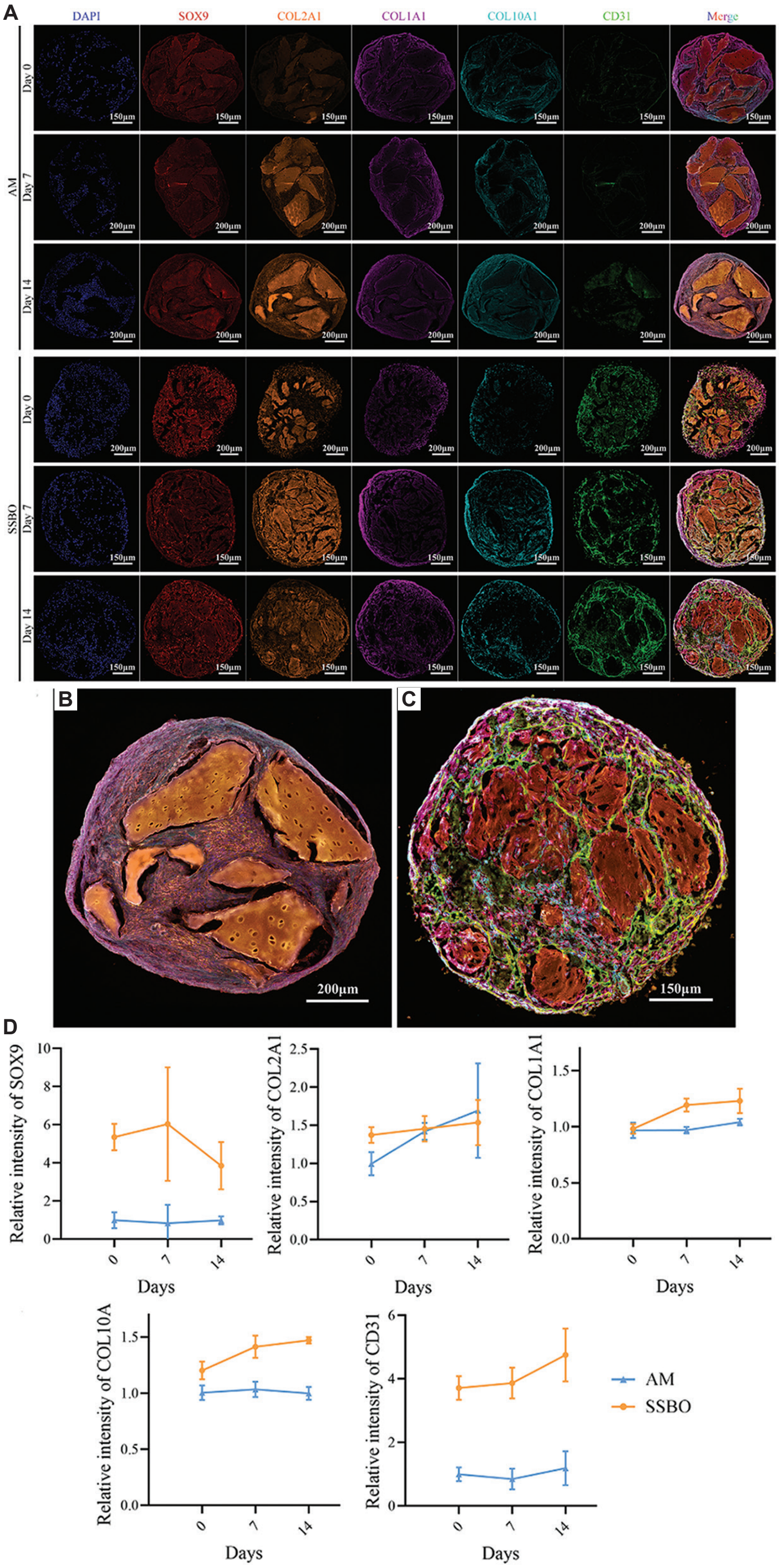

Figure 5. Differentiation of Organoids. (A) Representative multicolor immunofluorescence images of SSBO and AM on days 0, 7, and 14 of culture. From left to right: nuclear staining (DAPI), chondrogenic markers (SOX9, COL2A1), osteogenic markers(COL1A1), hypertrophic chondrocyte marker(COL10A1), endothelial cell marker (CD31), and merged images (Merge). (B) High-magnification view of AM on day 14 of spheroid formation. (C) High-magnification view of SSBO on day 14 of spheroid formation. (D) Quantification of the relative intensity for each marker shown in (A)

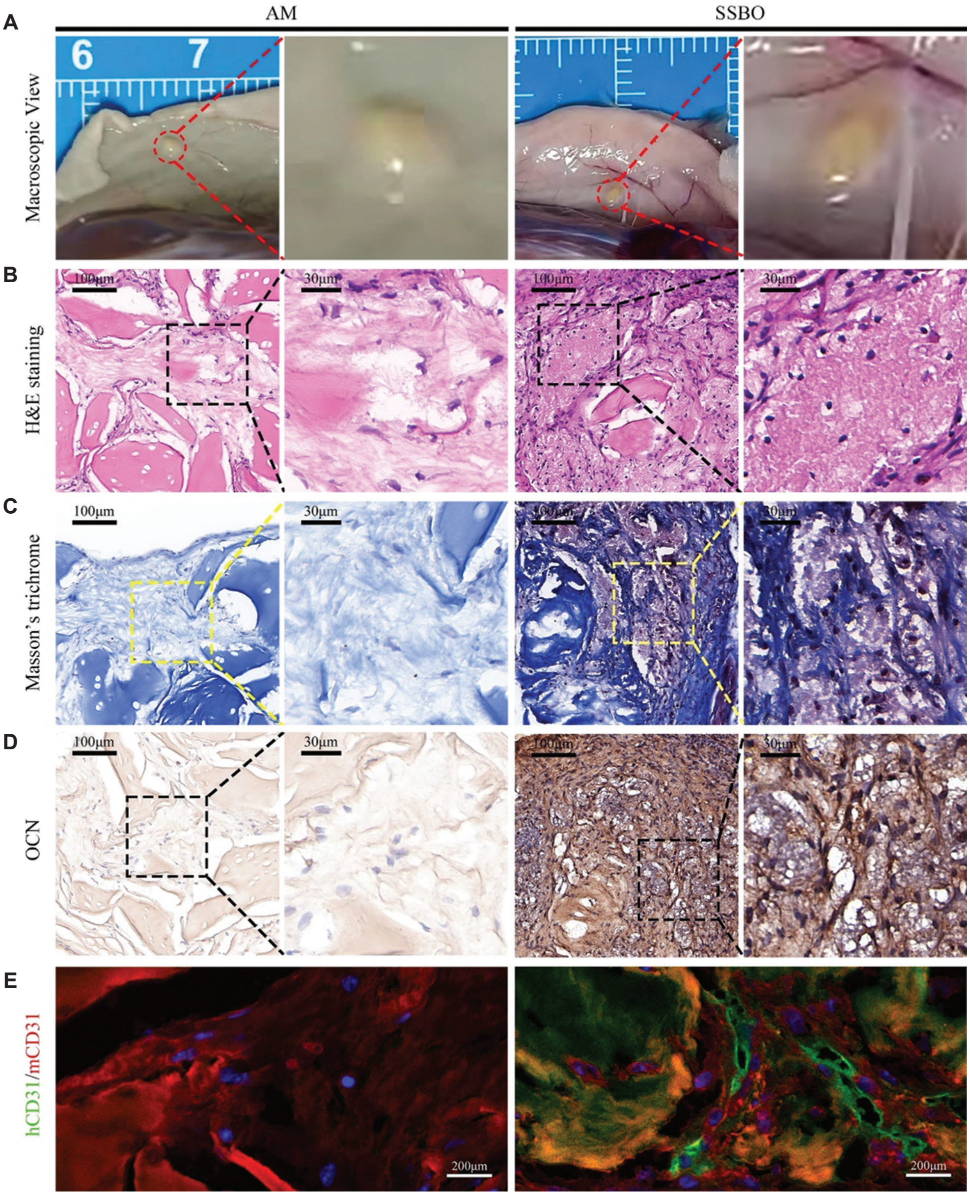

Figure 6. Evaluation of Ectopic Bone Formation After Subcutaneous Implantation for 3 Weeks. (A) epresentative macroscopic views of tissue regeneration in each group following 3 weeks of subcutaneous implantation in BALB/c nude mice. (B) H&E staining of explanted tissues. (C) Masson's trichrome staining. (D) Immunohistochemical staining for osteocalcin (OCN). (E) Immunofluorescence staining for human and murine CD31 to assess vascularization

SSBO can recruit and integrate into the host vascular system. In contrast, Minimal detection of murine CD31-positive endothelial cells was noted in the control group, with no observable vascular integration identified.

3.6. SSBO organoids promote repair of osteochondral defects and reconstruct subchondral bone structure in mice

To further evaluate the regenerative potential of SSBO organoids in bone tissue repair and osteochondral interface reconstruction, a mouse distal femoral osteochondral defect model was established. The defect measured approximately 0.8 mm in diameter and 1.0 mm in depth. Experimental animals were randomly assigned to four groups: blank control, AM group, SSBO group, and sham-operated group. Samples were harvested at 4 weeks post-surgery for evaluation.

Macroscopic observations showed that the blank control group exhibited a pronounced depression at the defect site, with a rough surface and slow repair progression. In the AM group, the defect was partially filled, but the surface remained irregular. In contrast, the

SSBO group demonstrated complete coverage of the defect with regenerated tissue, a smooth surface, and a color closely matching the surrounding cartilage, indicating a more favorable reconstruction outcome.Micro-CT analysis further confirmed these findings (Figure 7A). The SSBO group displayed substantial new bone formation, with the defect area nearly fully filled. The AM group showed partial filling of the defect, while the blank group exhibited minimal signs of healing. Quantitative analysis (Figure 7B) revealed that the bone volume to tissue volume ratio

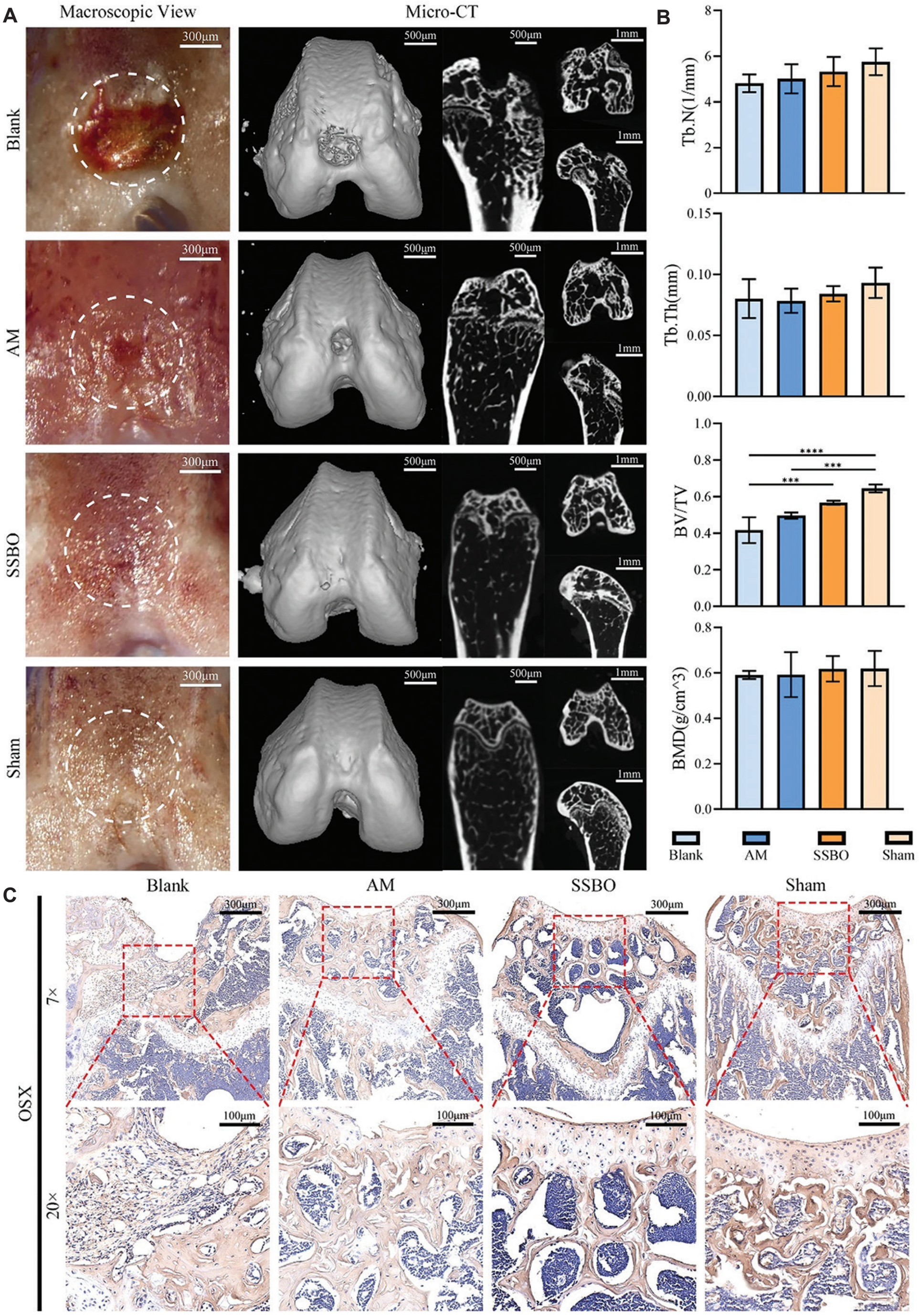

Figure 7. Evaluation of Osteochondral Regeneration After 4 Weeks of Implantation. (A) Morphological appearance of osteochondral repair in each group, 4 weeks post-implantation, and micro-CT images of the regenerated tissue, including overall 3D reconstruction, coronal view, transverse (axial) view, and sagittal view. (B) Quantitative analysis based on micro-CT, showing trabecular number (Tb.N), trabecular thickness (Tb.Th), bone volume to total volume ratio (BV/TV), and bone mineral density (BMD). (C) Immunohistochemical staining for Osterix (OSX) in regenerated bone tissue. Data are presented as mean ± SD (*n* = 4). **p* < 0.05, ***p* < 0.01, ****p* < 0.001. Key structures are annotated in the images: NB = new bone, RC = regenerated cartilage, FT = fibrous tissue

(BV/TV) in the SSBO group was significantly higher than in the blank group. Although slightly lower than that of the sham-operated group, the difference was not statistically significant. Furthermore, the SSBO group demonstrated superior performance in other structural parameters, quantitative assessment was performed on bone mineral density (BMD) and structural parameters, including trabecular thickness (Tb.Th) and trabecular number (Tb.N), compared with both the AM and blank groups, and approached the levels observed in the sham group.

Immunohistochemical staining (Figure 7C) revealed widespread and intense osterix (OSX)-positive signals in the implantation region of the SSBO group, with expression levels significantly higher than those observed in the AM (p=0.0028) and blank control (p=0.001) groups, and comparable to the sham-operated group. Quantitative analysis further confirmed these findings: although a difference remained between the SSBO and sham groups, the OSX expression in the SSBO group was notably higher than in the other groups (Figure S5C). These results suggest that SSBO possess a significant advantage in promoting the maturation of subchondral bone tissue.

Histological analysis further confirmed the experimental findings. H&E staining showed that the SSBO group developed a large number of well-aligned newly formed bone trabeculae, and the regenerated osteochondral tissue closely resembled native architecture (Figure 8A). Masson's trichrome staining revealed abundant collagen fiber deposition in the SSBO group, indicating robust matrix reconstruction (Figure 8B). Safranin O staining demonstrated that the regenerated cartilage layer was uniform, continuous, and of appropriate thickness, comparable to the sham group (Figure 8C). Conversely, the Blank and AM groups were mainly filled with fibrous tissue, with discontinuous bone structures and incomplete or collapsed cartilage layers. To quantitatively evaluate the quality of osteochondral defect repair, histological sections were assessed using the O'Driscoll scoring system. The SSBO group exhibited significantly higher scores compared to both the control group ($p < 0.0001$) and the AM group ($p = 0.0025$), indicating a superior tissue regeneration outcome (Figure S5D). Taken together, The results demonstrate that SSBO facilitates subchondral bone regeneration and supports the formation of structurally intact and morphologically appropriate articular cartilage. Notably, the findings further indicate that effective cartilage regeneration relies heavily on the functional restoration of the subchondral bone.

4. Discussion

The SCB is a structurally complex and functionally active component of the joint microenvironment. It has been increasingly recognized for its critical role in the initiation and progression of OA.[18] Beyond providing mechanical support and load buffering, SCB contributes to joint homeostasis by regulating osteochondral interface signaling, microvascular stability, and immune responses.[17,35] However, most current organoid models focus on single tissue types and fail to recapitulate the multicellular, multi-functional microenvironment of SCB. The development of a three-dimensional *in vitro* model that integrates angiogenic, immunomodulatory, and osteogenic functions remains a significant challenge in tissue engineering and disease modeling.[36-38]

In this study, we successfully constructed an SSBO by leveraging the intrinsic cellular heterogeneity of SVF and a CECM scaffold. Unlike conventional approaches that rely on single-cell populations such as ADSCs or BMSCs, SVF comprises a diverse set of functional subtypes—including EPCs, MSCs, macrophages, and pericytes—endowing it with pro-vascular, mesenchymal, and immunoregulatory potential.[39-41] Flow cytometry confirmed the presence of these subpopulations, while histological and ultrastructural analyses demonstrated their active participation in scaffold colonization and tissue remodeling.

Beyond self-assembly, SSBO exhibited dynamic matrix remodeling driven by coordinated interactions between ADSCs and macrophages. SVF-derived cells not only adhered to the CECM surface but also infiltrated deeply into the scaffold, accompanied by localized degradation and collagen deposition. ADSCs are known to secrete matrix metalloproteinases (MMPs), which initiate the enzymatic breakdown of the extracellular matrix.[42,43] Meanwhile, infiltrating CD68$^+$ macrophages may facilitate debris clearance and immune modulation by releasing cytokines and undergoing phenotype switching.[44-46] Transmission electron microscopy revealed abundant mitochondria and endoplasmic reticulum in SSBO cells, indicating enhanced metabolic and biosynthetic activity, in contrast to stress-associated lysosomal features observed in AM controls. Based on these findings, we propose a three-step remodeling model: enzymatic degradation by ADSCs, immune clearance by macrophages, and collaborative matrix reconstruction. Importantly, ADSCs can also secrete immunomodulatory factors such as IL-6, PGE2, and TGF-β to promote macrophage polarization toward the M2 phenotypemost.[47-48] We found macrophages in SSBO were found around the edge of the organoid-like areas. They showed high levels of IL-10, which points to an anti-inflammatory state. IL-1β levels rose first and then fell. The IL-10/IL-1β ratio peaked on day 7 and was much higher than in the control group. This suggests that macrophages may shift toward an M2-like state, helping balance the immune system and supporting repair. However, this study only used indirect markers to

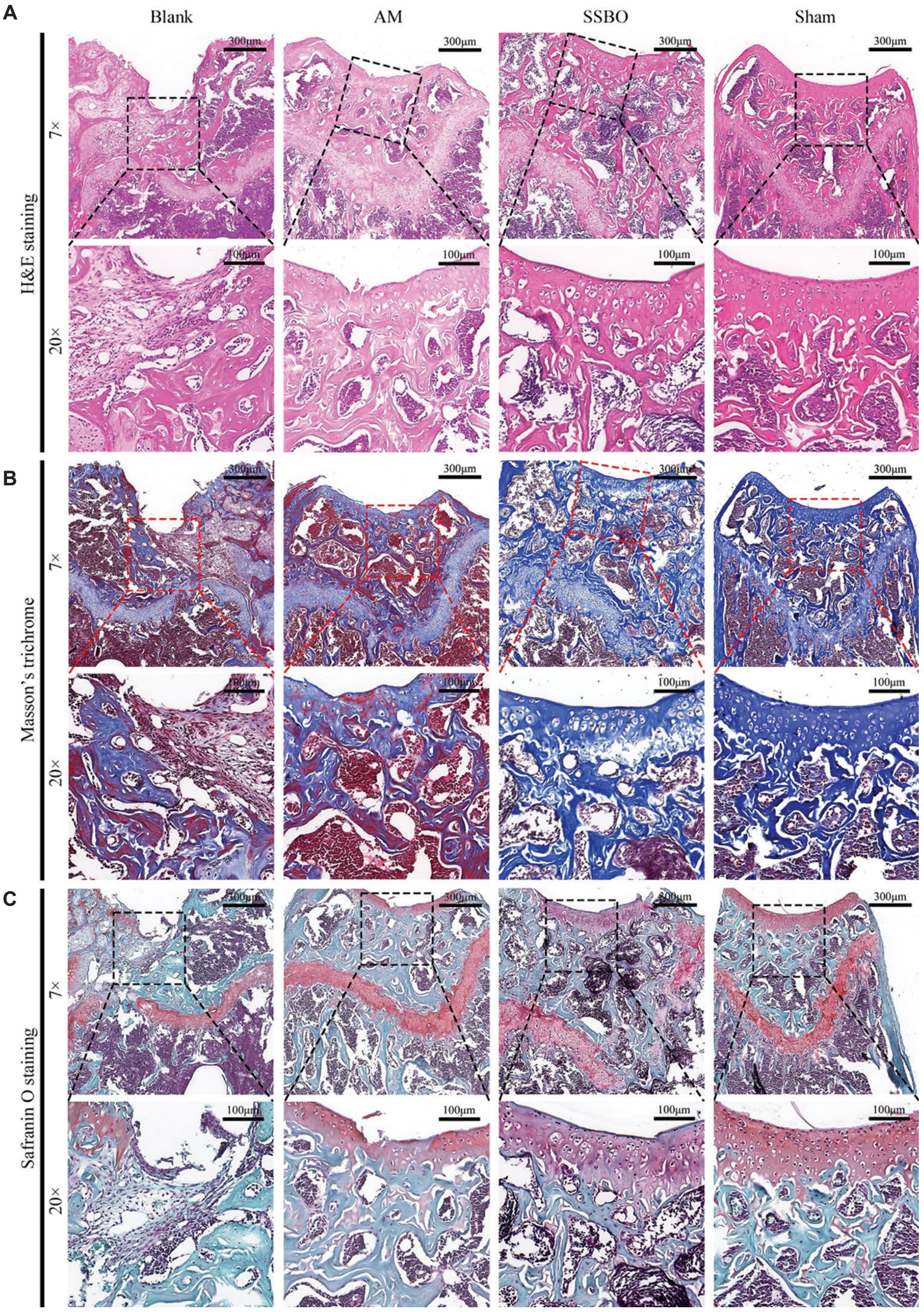

Figure 8. Histological Staining at 4 Weeks Post-Implantation. (A) H&E staining of regenerated tissues. (B) Masson's trichrome staining. (C) Safranin O staining of the implanted constructs at 4 weeks post-implantation. Key structures are annotated in the images: NB = new bone, RC = regenerated cartilage, FT = fibrous tissue

identify M2-like macrophages. Direct markers, such as CD206 and Arg1, were not tested. Future work should include a broader set of markers using immunostaining or gene analysis. Cytokine profiling and functional tests are also needed. These steps will help define the exact role of macrophages in tissue repair and reveal how they interact with ADSCs.

A hallmark of SSBO is its intrinsic ability to form vascular-like networks *in vitro*, independent of exogenous angiogenic stimulation. Multiplex immunostaining revealed that CD31$^+$ EPCs aligned along scaffold channels, forming structured tubular networks by day 14. These were accompanied by PDGFRβ$^+$ pericytes, which did not co-localize with endothelial cells but were positioned adjacent to them, suggesting vessel stabilization through paracrine signaling. Interestingly, we observed a mismatch between VEGF and CD31 expression at the mRNA and protein levels. This may result from post-transcriptional regulation, protein stability differences, or spatial heterogeneity within the organoid. These findings reflect the complexity of self-organization and local regulation in organoid systems. In contrast, AM organoids showed limited spatial organization and lacked vascular markers. The vascularization observed in SSBO is likely orchestrated by the synergistic actions of SVF-derived cell types: EPCs initiate vessel formation, ADSCs enhance angiogenesis through VEGF and bFGF secretion, and M2-like macrophages promote maturation and extracellular matrix remodeling. Pericytes may further stabilize nascent vessels via PDGF and Angiopoietin signaling.[47-50] This multicellular coordination leads to spatially organized, functional vasculature that supports both perfusion and structural development of the organoid.

Importantly, SSBO also exhibited characteristics of vascular–osteogenic coupling, closely resembling the physiological process of endochondral ossification. Gene and protein expression analyses demonstrated sequential activation of chondrogenic (SOX9, COL2A1), hypertrophic (COL10A1), and osteogenic (RUNX2, COL1A1, OCN) markers. Notably, COL10A1$^+$ hypertrophic zones were spatially adjacent to CD31$^+$ vascular structures, suggesting synchronized cartilage maturation and angiogenesis. This coupling likely enhances nutrient exchange, cell differentiation, and matrix remodeling, thus improving scaffold integration and tissue maturation. In vivo, SSBO constructs formed chimeric human-mouse vasculature and exhibited superior osteogenic marker expression and bone-like matrix deposition compared to controls. In a mouse osteochondral defect model, SSBO facilitated the simultaneous regeneration of cartilage and subchondral bone, resulting in near-native tissue architecture. These findings underscore the importance of multicellular interactions in orchestrating vascular, immune, and osteogenic processes essential for effective osteochondral repair.

Despite the promising results, several limitations should be acknowledged. First, as a natural biomaterial, CECM may exhibit batch-to-batch variability, necessitating standardized quality control measures for future applications. Second, although SVF contains multiple functional subpopulations, their specific roles in tissue reconstruction have not been directly confirmed by lineage tracing or functional blockade studies. Third, transcriptomic and proteomic analyses were not performed, limiting our understanding of the molecular mechanisms underlying SSBO self-organization. Finally, in vivo evaluations were conducted in immunodeficient mice; further validation in large-animal models is required to assess clinical translatability.

5. Conclusion

This study presents a novel approach for constructing subchondral bone organoids by combining SVF with CECM scaffolds. The resulting SSBO exhibit self-organization, multi-lineage differentiation, vascular integration, and immune modulation. These organoids not only mimic the spatial and functional complexity of native SCB but also demonstrate significant regenerative potential in vivo. This approach holds strong potential for clinical application. SVF cells are autologous, can be harvested intraoperatively, and do not require additional growth factors or genetic modification. These features make SSBO a simple, efficient, and scalable strategy. Furthermore, the SSBO platform can be applied in studies of bone immunology, personalized therapies for joint disorders, and disease modeling. It provides a promising avenue for future precision medicine in tissue regeneration.

Acknowledgments

None.

Funding

This study was supported by the National Key Research and Development Program of China (Grant No. 2024YFA1108600).

Conflict of interest

The authors declare no competing financial interests.

Author contributions

Conceptualization: Jiazhou Wu, Zexian Liu, Aiyuan Wang, Hongyu Jiang, Yun Bai
Formal analysis: Tao Qian, Jiazhou Wu, Zexian Liu, Junli Wang, Biao Ma, Jialiang You
Investigation: Zexian Liu, Aiyuan Wang, Yanbin Wu, Zhengrui Zhou, Cheng Huang
Methodology: Tao Qian, Yanbin Wu, Junli Wang, Hongyu Jiang, Zhengrui Zhou, Endong Luo
Writing–original draft: Tao Qian, Jiazhou Wu, Cheng Huang, Junming Zhang, Dingkai Wang
Writing–review & editing: Tao Qian, Yazhou Li, Ying He, Jiang Peng

Ethics approval and consent to participate

This study involving human participants was approved by the Ethics Committee of the Chinese PLA General Hospital (Approval No. 2023KY088-KS001). Adipose tissue samples were collected from 9 patients who underwent liposuction at the Fourth Medical Center of the Chinese PLA General Hospital. All participants provided written informed consent prior to inclusion in the study. None of the participants had a history of metabolic or endocrine disorders, alcohol abuse, smoking, or the use of medications affecting glucose or lipid metabolism. All procedures involving human participants were conducted in accordance with the Declaration of Helsinki and the relevant institutional and national ethical guidelines.

Consent for publication

Written informed consent was obtained from all participants prior to their inclusion in the study. Each participant explicitly agreed to the use of their clinical samples for research purposes. No personally identifiable information or images of human subjects are included in the manuscript.

Availability of data

The data that support the findings of this study are available from the corresponding author upon reasonable request.

References

1. Bijlsma JW, Berenbaum F, Lafeber FP. Osteoarthritis: an update with relevance for clinical practice. *Lancet (London, England)*. Jun 18 2011;377(9783):2115-2126.

   doi: 10.1016/s0140-6736(11)60243-2

2. GBD 2017 Disease and Injury Incidence and Prevalence Collaborators. Global, regional, and national incidence, prevalence, and years lived with disability for 354 diseases and injuries for 195 countries and territories, 1990-2017: a systematic analysis for the Global Burden of Disease Study 2017. *Lancet (London, England)*. Nov 10 2018;392(10159):1789-1858.

   doi: 10.1016/s0140-6736(18)32279-7

3. Reichenbach S, Felson DT, Hincapié CA, *et al*. Effect of Biomechanical Footwear on Knee Pain in People With Knee Osteoarthritis: The BIOTOK Randomized Clinical Trial. *Jama*. May 12 2020;323(18):1802-1812.

   doi: 10.1001/jama.2020.3565

4. Martel-Pelletier J, Barr AJ, Cicuttini FM, *et al*. Osteoarthritis. *Nature reviews Disease primers*. Oct 13 2016;2:16072.

   doi: 10.1038/nrdp.2016.72

5. Grynpas MD, Alpert B, Katz I, Lieberman I, Pritzker KP. Subchondral bone in osteoarthritis. *Calcified tissue international*. Jul 1991;49(1):20-26.

   doi: 10.1007/bf02555898

6. Burr DB, Gallant MA. Bone remodelling in osteoarthritis. *Nature reviews Rheumatology*. Nov 2012;8(11):665-673.

   doi: 10.1038/nrrheum.2012.130

7. Suri S, Walsh DA. Osteochondral alterations in osteoarthritis. *Bone*. Aug 2012;51(2):204-211.

   doi: 10.1016/j.bone.2011.10.010

8. Goldring SR, Goldring MB. Changes in the osteochondral unit during osteoarthritis: structure, function and cartilage-bone crosstalk. *Nature reviews Rheumatology*. Nov 2016;12(11):632-644.

   doi: 10.1038/nrrheum.2016.148

9. Karsdal MA, Bay-Jensen AC, Lories RJ, *et al*. The coupling of bone and cartilage turnover in osteoarthritis: opportunities for bone antiresorptives and anabolics as potential treatments? *Annals of the rheumatic diseases*. Feb 2014;73(2):336-348.

   doi: 10.1136/annrheumdis-2013-204111

10. Zhang H, Wang L, Cui J, *et al*. Maintaining hypoxia environment of subchondral bone alleviates osteoarthritis progression. *Science advances*. Apr 5 2023;9(14):eabo7868.

    doi: 10.1126/sciadv.abo7868

11. Chen Z, Bo Q, Wang C, Xu Y, Fei X, Chen R. Single BMSC-derived cartilage organoids for gradient heterogeneous osteochondral regeneration by leveraging native vascular microenvironment. *Journal of nanobiotechnology*. Apr 29 2025;23:325.

    doi: 10.1186/s12951-025-03403-0

12. Lyu X, Wang J, Su J. Intelligent Manufacturing for Osteoarthritis Organoids. *Cell proliferation*. Jul 2025;58(7):e70043.

    doi: 10.1111/cpr.70043

13. Day JS, Ding M, van der Linden JC, Hvid I, Sumner DR, Weinans H. A decreased subchondral trabecular bone tissue elastic modulus is associated with pre-arthritic cartilage damage. *Journal of orthopaedic research: official publication of the Orthopaedic Research Society*. Sep 2001;19(5):914-918.

    doi: 10.1016/s0736-0266(01)00012-2

14. Hu W, Chen Y, Dou C, Dong S. Microenvironment in subchondral bone: predominant regulator for the treatment of osteoarthritis. *Annals of the rheumatic diseases*. Apr 2021;80(4):413-422.

    doi: 10.1136/annrheumdis-2020-218089

15. Hu Y, Chen X, Wang S, Jing Y, Su J. Subchondral bone microenvironment in osteoarthritis and pain. *Bone research*. Mar 17 2021;9(1):20.

    doi: 10.1038/s41413-021-00147-z

16. Song H, Li X, Zhao Z, *et al*. Reversal of Osteoporotic Activity by Endothelial Cell-Secreted Bone Targeting and Biocompatible Exosomes. *Nano letters*. May 8 2019;19(5):3040-3048.

    doi: 10.1021/acs.nanolett.9b00287

17. Castañeda S, Roman-Blas JA, Largo R, Herrero-Beaumont G. Subchondral bone as a key target for osteoarthritis treatment. *Biochemical pharmacology*. Feb 1 2012;83(3):315-323.

    doi: 10.1016/j.bcp.2011.09.018

18. Li G, Yin J, Gao J, *et al*. Subchondral bone in osteoarthritis: insight into risk factors and microstructural changes. *Arthritis research & therapy*. 2013;15(6):223.

doi: 10.1186/ar4405

19. Henrotin Y, Pesesse L, Sanchez C. Subchondral bone and osteoarthritis: biological and cellular aspects. *Osteoporosis international*. Dec 2012;23 (Suppl 8):847-851.

    doi: 10.1007/s00198-012-2162-z

20. Kim W, Gwon Y, Park S, Kim H, Kim J. Therapeutic strategies of three-dimensional stem cell spheroids and organoids for tissue repair and regeneration. *Bioactive materials*. Jan 2023;19:50-74.

    doi: 10.1016/j.bioactmat.2022.03.039

21. Hofer M, Lutolf MP. Engineering organoids. *Nature reviews Materials*. 2021;6(5):402-420.

    doi: 10.1038/s41578-021-00279-y

22. Takebe T, Sekine K, Enomura M, *et al*. Vascularized and functional human liver from an iPSC-derived organ bud transplant. *Nature*. Jul 25 2013;499(7459):481-484.

    doi: 10.1038/nature12271

23. Lancaster MA, Renner M, Martin CA, *et al*. Cerebral organoids model human brain development and microcephaly. *Nature*. Sep 19 2013;501(7467):373-379.

    doi: 10.1038/nature12517

24. Takasato M, Er PX, Chiu HS, *et al*. Kidney organoids from human iPS cells contain multiple lineages and model human nephrogenesis. *Nature*. Oct 22 2015;526(7574):564-568.

    doi: 10.1038/nature15695

25. Zhang C, Jing Y, Wang J, *et al*. Skeletal organoids. *Biomaterials translational*. 2024;5(4):390-410.

    doi: 10.12336/biomatertransl.2024.04.005

26. Zakhari JS, Zabonick J, Gettler B, Williams SK. Vasculogenic and angiogenic potential of adipose stromal vascular fraction cell populations *in vitro*. *In vitro cellular & developmental biology Animal*. Jan 2018;54(1):32-40.

    doi: 10.1007/s11626-017-0213-7

27. Reid G, Cerino G, Melly L, *et al*. Harnessing the angiogenic potential of adipose-derived stromal vascular fraction cells with perfusion cell seeding. *Stem cell research & therapy*. May 1 2025;16:220.

    doi: 10.1186/s13287-025-04286-6

28. Moreira HR, Rodrigues DB, Freitas-Ribeiro S, *et al*. Spongy-like hydrogels prevascularization with the adipose tissue vascular fraction delays cutaneous wound healing by sustaining inflammatory cell influx. *Materials today Bio*. Dec 15 2022;17:100496.

    doi: 10.1016/j.mtbio.2022.100496

29. Liu W, Jiang H, Chen J, *et al*. High paracrine activity of hADSCs cartilage microtissues inhibits extracellular matrix degradation and promotes cartilage regeneration. *Materials today Bio*. Feb 2025;30:101372.

    doi: 10.1016/j.mtbio.2024.101372

30. Kim YS, Majid M, Melchiorri AJ, Mikos AG. Applications of decellularized extracellular matrix in bone and cartilage tissue engineering. *Bioengineering & translational medicine*. Jan 2019;4(1):83-95.

    doi: 10.1002/btm2.10110

31. Morris AH, Stamer DK, Kyriakides TR. The host response to naturally-derived extracellular matrix biomaterials. *Seminars in immunology*. Feb 2017;29:72-91.

    doi: 10.1016/j.smim.2017.01.002

32. Liu C, Pei M, Li Q, Zhang Y. Decellularized extracellular matrix mediates tissue construction and regeneration. *Frontiers of medicine*. Feb 2022;16(1):56-82.

    doi: 10.1007/s11684-021-0900-3

33. Zhang X, Chen X, Hong H, Hu R, Liu J, Liu C. Decellularized extracellular matrix scaffolds: Recent trends and emerging strategies in tissue engineering. *Bioactive materials*. Apr 2022;10:15-31.

    doi: 10.1016/j.bioactmat.2021.09.014

34. Guo X, Liu B, Zhang Y, *et al*. Decellularized extracellular matrix for organoid and engineered organ culture. *Journal of tissue engineering*. Jan-Dec 2024;15:20417314241300386.

    doi: 10.1177/20417314241300386

35. Pan J, Zhou X, Li W, Novotny JE, Doty SB, Wang L. In situ measurement of transport between subchondral bone and articular cartilage. *Journal of orthopaedic research*. Oct 2009;27(10):1347-1352.

    doi: 10.1002/jor.20883

36. Verdugo-Avello F, Wychowaniec JK, Villacis-Aguirre CA, D'Este M, Toledo JR. Bone microphysiological models for biomedical research. *Lab on a chip*. Feb 25 2025;25(5):806-836.

    doi: 10.1039/d4lc00762j

37. Wang J, Wu Y, Li G, *et al*. Engineering Large-Scale Self-Mineralizing Bone Organoids with Bone Matrix-Inspired Hydroxyapatite Hybrid Bioinks. *Advanced materials (Deerfield Beach, Fla)*. Jul 2024;36(30):e2309875.

    doi: 10.1002/adma.202309875

38. Zhang X, Jiang W, Wu X, *et al*. Divide-and-conquer strategy with engineered ossification center organoids for rapid bone healing through developmental cell recruitment. *Nature communications*. Jul 4 2025;16:6200.

    doi: 10.1038/s41467-025-61619-y

39. Bora P, Majumdar AS. Adipose tissue-derived stromal vascular fraction in regenerative medicine: a brief review on biology and translation. *Stem cell research & therapy*. Jun 15 2017;8(1):145.

    doi: 10.1186/s13287-017-0598-y

40. Rehman J, Traktuev D, Li J, *et al*. Secretion of angiogenic and antiapoptotic factors by human adipose stromal cells. *Circulation*. Mar 16 2004;109(10):1292-1298.

doi: 10.1161/01.Cir.0000121425.42966.F1

41. Wu J, He Y, Qian T, *et al*. Stromal vascular fraction self-assembles vascularized osteogenic organoids with immunomodulatory functions. *Bioactive materials*. 2026/03/01/2026;57:323-343.

    doi: 10.1016/j.bioactmat.2025.10.030

42. Ahmad N, Anker A, Klein S, *et al*. Autologous Fat Grafting-A Panacea for Scar Tissue Therapy? *Cells*. Aug 20 2024;13(16)

    doi: 10.3390/cells13161384

43. Airuddin SS, Halim AS, Wan Sulaiman WA, Kadir R, Nasir NAM. Adipose-Derived Stem Cell: "Treat or Trick". *Biomedicines*. Nov 5 2021;9(11)

    doi: 10.3390/biomedicines9111624

44. Guan F, Wang R, Yi Z, *et al*. Tissue macrophages: origin, heterogenity, biological functions, diseases and therapeutic targets. Signal transduction and targeted therapy. Mar 7 2025;10(1):93.

    doi: 10.1038/s41392-025-02124-y

45. Uribe-Querol E, Rosales C. Phagocytosis: Our Current Understanding of a Universal Biological Process. *Frontiers in immunology*. 2020;11:1066.

    doi: 10.3389/fimmu.2020.01066

46. Blanchard L, Girard JP. High endothelial venules (HEVs) in immunity, inflammation and cancer. *Angiogenesis*. Nov 2021;24(4):719-753.

    doi: 10.1007/s10456-021-09792-8

47. Mohan SP, Priya SP, Tawfig N, *et al*. The Potential Role of Adipose-Derived Stem Cells in Regeneration of Peripheral Nerves. Neurology international. Feb 6 2025;17(2)

    doi: 10.3390/neurolint17020023

48. Xiong J, Qiang H, Li T, *et al*. Human adipose-derived stem cells promote seawater-immersed wound healing via proangiogenic effects. *Aging*. Mar 26 2021; 13(13):17118-17136.

    doi: 10.18632/aging.202773

49. Li J, Liu Y, Zhang R, *et al*. Insights into the role of mesenchymal stem cells in cutaneous medical aesthetics: from basics to clinics. *Stem cell research & therapy*. Jun 18 2024;15(1):169.

    doi: 10.1186/s13287-024-03774-5

50. Vanderstichele S, Vranckx JJ. Anti-fibrotic effect of adipose-derived stem cells on fibrotic scars. *World journal of stem cells*. Feb 26 2022;14(2):200-213.

    doi: 10.4252/wjsc.v14.i2.200